Cross section and induced polarization in ^{3}He elastic scattering at 443 MeV

J. Kamiya,[1,*] K. Hatanaka,[1,2,†] T. Adachi,[2] K. Fujita,[1] K. Hara,[1] T. Kawabata,[3] T. Noro,[4] H. Sakaguchi,[5] N. Sakamoto,[1] Y. Sakemi,[1] Y. Shimbara,[2] Y. Shimizu,[1] S. Terashima,[5] M. Uchida,[5] T. Wakasa,[1,‡] Y. Yasuda,[5] H. P. Yoshida,[1] and M. Yosoi[5]

[1]*Research Center for Nuclear Physics, Osaka University, Ibaraki, Osaka 567-0047, Japan*

[2]*Department of Physics, Osaka University, Toyonaka, Osaka 560-0043, Japan*

[3]*Center for Nuclear Study, University of Tokyo, Bunkyo, Tokyo 113-0033, Japan*

[4]*Department of Physics, Kyushu University, Hakozaki, Fukuoka 812-8581, Japan*

[5]*Department of Physics, Kyoto University, Kyoto 606-8502, Japan*

(Received 24 March 2003; published 27 June 2003)

Angular distributions of the differential cross section and the induced polarization of ^{3}He elastic scattering on ^{12}C, ^{58}Ni, and ^{90}Zr targets were measured at 443 MeV incident energy. This is the first measurement of ^{3}He spin observables at intermediate energies. Cross sections and polarizations were measured in the range of center-of-mass angles of 5°–30° and 5°–20°, respectively. The polarization was measured with the focal plane polarimeter system of the Grand Raiden spectrometer, which was calibrated for ^{3}He at the present energy. The optical potential parameters including the spin-orbit term were determined by a systematic search procedure. The diffuseness parameter of the spin-orbit potential was about 0.6–0.8 fm in contrast to much smaller values of 0.2–0.3 fm reported at lower energies. The energy dependence of the reduced volume integrals of the optical potential was found to be similar to that observed for protons at intermediate energies, but the real potential terms were smaller. Single folding (SF) model calculations were performed and compared with the experimental data. We found that the renormalization factors used to modify the SF potential were necessary in order to obtain a good fit to the data. These results call for an appropriate density dependent nucleon-nucleus interaction in the ^{3}He nucleus.

DOI: 10.1103/PhysRevC.67.064612 PACS number(s): 25.55.Ci, 24.10.Ht, 24.70.+s

I. INTRODUCTION

One of the main subjects in nuclear physics is the understanding of the nature of nuclear interactions and nuclear phenomena based on the fundamental Hamiltonian. A new generation of realistic nucleon-nucleon (NN) interactions was developed by using meson exchange or other more phenomenological approaches [1–3]. These realistic two-nucleon forces were successfully applied in the studies of few-nucleon systems where rigorous solutions of the Schrödinger equation were available (see Refs. [4,5], and references therein). Nucleon- and nucleus-nucleus scattering have been studied well in the framework of both nonrelativistic and relativistic equations. Although the Hamiltonian of a system can be written down for a many-body system, the strict solution cannot be obtained except for few-body systems. One approach of solving the many-body Schrödinger equation was to obtain the interaction by folding an effective NN interaction with the nucleon densities of the colliding nuclei. In this folding model approach, various effective interactions [6–8] and their modifications in the nuclear matter [9] were investigated. To include the medium modification, density dependent effective interactions were introduced in the description of the elastic scattering of light [10–12] and heavy ions [13,14]. These density dependent interactions were developed with finite-range exchange terms to provide basic nuclear properties such as the binding energy of cold nuclear matter at the saturation density [15,16].

Spin-dependent interactions in nucleon- and nucleus-nucleus scattering are of special interest because they are closely related to both the nuclear structure and the reaction mechanism. Extensive studies of the spin-dependent interaction of protons and deuterons became possible due to the development of efficient polarized ion sources and sophisticated polarimeters. These experimental as well as theoretical studies of many proton and deuteron polarization observables cover a wide range of incident energies from sub-MeV to several tens of GeV on a variety of nuclei (see Refs. [17–22], and references therein). On the other hand, for heavier projectiles with mass numbers $A \geqslant 3$, measurements of polarization observables are limited to low energies due to the lack of polarized ion beams, for example, ^{3}H ($E_{\rm lab} \leqslant 17$ MeV) [23,24], ^{3}He ($E_{\rm lab} = 33$ MeV) [25,26], and ^{6,7}Li ($E_{\rm lab} \leqslant 50$ MeV) [27,28]. Many interesting results were obtained from these studies. The optical model analyses of ^{3}He elastic scattering at 33 MeV showed an anomalous peculiarity that the diffuseness parameters of the spin-orbit potential were extremely small, i.e., between 0.2 and 0.3 fm. The resulting spin-orbit potential depths between 2 and 4 MeV are comparable with those expected from the simple folding model [25,26]. The ^{3}He spin-orbit potential seemed sharply localized at the nuclear surface. In contrast, the spin-orbit diffuseness parameters of tritons were found to be larger than those of ^{3}He and similar to those of protons ($a_{\rm so} \geqslant 0.4$ fm) [24,29]. Since the unpaired nucleon is a neutron for ^{3}He and a proton for tritons, the difference in the diffuseness param-

*Present address: Japan Atomic Energy Research Institute, Tokai, Ibaraki 319-1195, Japan. Electronic address: kamiya@linac.tokai.jaeri.go.jp

†Electronic address: hatanaka@rcnp.osaka-u.ac.jp

‡Present address: Department of Physics, Kyushu University, Hakozaki, Fukuoka 812-8581, Japan.

 ©2003 The American Physical Society

eters could represent an isospin effect of the spin-orbit potentials. However, it should be noted that the optical potential parameters had, in general, large ambiguities at low energies and could not be determined uniquely. For ^{3}He-nucleus elastic scattering at intermediate energies, where only differential cross sections were measured, optical model calculations showed that the data were well reproduced without a spin-orbit term [30]. The spin-orbit term of the optical potential is therefore experimentally not yet determined.

A volume integral of a potential that is not significantly affected by a continuous ambiguity [31] of each potential parameter was proposed to investigate the systematic behavior of the optical potential. However, so-called discrete ambiguities remained in the ^{3}He optical potential parameters at low incident energies up to 40 MeV/nucleon [32]. Two different sets of parameters reproduced experimental data equally well. One of them gave larger values of the volume integral per nucleon of the real central potential, $J_R/A_PA_T \approx 440$ MeV fm^3 (deep potential), and the other gave smaller values ≈ 330 MeV fm^3 (shallow potential). The deep potential set was considered to be more realistic, because volume integrals calculated by folding nucleon-nucleus optical potentials were similar to those of the deep potential set. However, it was found that the shallow potential reproduces the data better at backward angles for incident energies around 30–40 MeV/nucleon. The investigation of volume integrals was extended to intermediate energies up to 150 MeV/nucleon [33]. The volume integrals of ^{3}He real central potentials were found to decrease with increasing incident energies above 70 MeV/nucleon. This energy dependence was similar to that of protons at intermediate energies, although the volume integrals for ^{3}He were slightly smaller than for protons by 25–30 % at 150 MeV/nucleon. This suggests that the ^{3}He-nucleus interaction could be roughly explained by the sum of the interactions between constituent nucleons in ^{3}He and the target nucleus. On the other hand, the imaginary potential of ^{3}He at 150 MeV/nucleon gave only half the value of the volume integral and generally also exhibited a different energy dependence than for protons. These results are not fully understood as yet. The above discussion, however, is only based on available cross section data for ^{3}He scattering. A ^{3}He particle with an incident energy of 150 MeV/nucleon has a large grazing angular momentum, e.g., nearly $60\hbar$ in a collision with a nucleus of mass number $A \sim 60$. The measurement of polarization observables is indispensable to better understand the interactions, since the spin-orbit potential, which can be pinned down by these observables, will affect the resulting central potentials.

Folding model optical potentials are widely accepted in microscopical descriptions of the elastic scattering of compound nuclei [34], because the nucleon-nucleus optical potentials in the single folding (SF) model, the nuclear densities, and the effective *NN* interactions in the double folding (DF) model are well known. Recently, the effects of the spin-orbit interactions on the elastic scattering of ^{3}He from heavy-mass nuclei at intermediate energies have been studied theoretically within the folding models [35]. Calculations showed that the spin-orbit interaction had a large effect on the differential cross section over a wide range of scattering angles. The predicted analyzing powers reached almost the maximal value of $A_y = 1$ at scattering angles around 20°–30° in the center-of-mass system. Such a large analyzing power could allow for reliable investigations of the spin-orbit interaction.

In the present study, we measured the angular distributions of the differential cross section and the induced polarization of elastically scattered ^{3}He on ^{12}C, ^{58}Ni, and ^{90}Zr targets at 443 MeV. In Sec. II, details of the experimental methods will be presented. In Sec. III, the experimental results are shown together with an optical model analysis that includes spin-orbit terms. In Sec. IV, the energy dependent volume integrals of the optical potential are discussed and compared to those of protons. We also compared the results of the single folding model calculations with the measurements. Summary and conclusions follow in Sec. V.

II. EXPERIMENTAL METHOD

The measurements were performed at the Research Center for Nuclear Physics, Osaka University. A ^{3}He^{2+} beam from an electron cyclotron resonance (ECR) ion source was accelerated to 93 MeV by a $K = 120$ MeV AVF (azimuthally varying field) cyclotron. The extracted beam was transported to a $K = 400$ MeV ring cyclotron and accelerated to 443 MeV. This beam was achromatically transported to the target in the scattering chamber of the Grand Raiden spectrometer [36] through the in the west experiment hall beam line [37]. The horizontal and vertical acceptance of the Grand Raiden spectrometer was set by a slit system to ± 10 and ± 40 mrad, respectively. The beam current was measured by a Faraday cup in the scattering chamber. The maximum beam current on the target was about 40 *e*nA. The energy resolution in the focal plane was 190 keV full width at half maximum due to the energy spread of the cyclotron beam because of the achromatic tuning of the WS beam line. In dispersive beam line mode, a higher resolution can be achieved [38], but for this experiment the present resolution was sufficient.

Figures 1 and 2 show the schematic layout of the Grand Raiden spectrometer and its focal plane (FP) detector and focal plane polarimeter (FPP) system [39], respectively. ^{3}He particles scattered from the target nuclei were momentum analyzed by the Grand Raiden spectrometer and detected in the FP detector system consisting of two multiwire drift chambers (MWDCs) [40] and a ΔE plastic scintillator (see Fig. 2). The MWDCs were designed to measure both the positions and the angles of particles in the horizontal and vertical planes. ^{3}He particles were identified by the time of flight information measured between trigger signals and the rf pickup of the AVF cyclotron. The polarization of elastically scattered ^{3}He particles was determined in the FPP system by measuring the left-right asymmetry downstream of a second scatterer. The FPP system consisted of four MW proportional chambers (MWPCs), the second scatterer as an ''analyzer,'' and a calorimeter which was specially designed for this experiment. Events scattered from the analyzer were selected using the vertex position along the central orbit of the spectrometer, where the distance between the trajectories

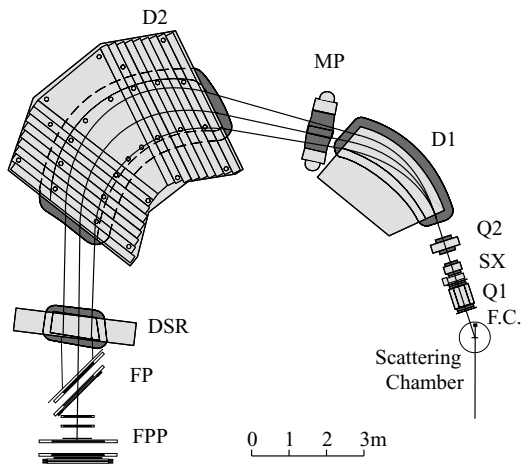

FIG. 1. Schematic layout of the Grand Raiden spectrometer and its FP detector and FPP system.

before and after the analyzer was minimum. The calorimeter was designed to measure the total energy of the ^{3}He particles scattered by the analyzer. It consisted of three planes of plastic scintillators and was thick enough to stop all ^{3}He particles. The total energy was obtained by summing the energies deposited in the scintillators. ^{3}He particles scattered in the analyzer were identified using the ΔE information in the first plane of the calorimeter.

A. Effective analyzing power of the ^{3}He polarimeter

Before the polarization measurements, the effective analyzing power of the FPP system was determined for ^{3}He. Details of this calibration are described in Ref. [41]. Here, we will summarize the procedure and results. ^{3}He particles were polarized by scattering on the first target "polarizer." In

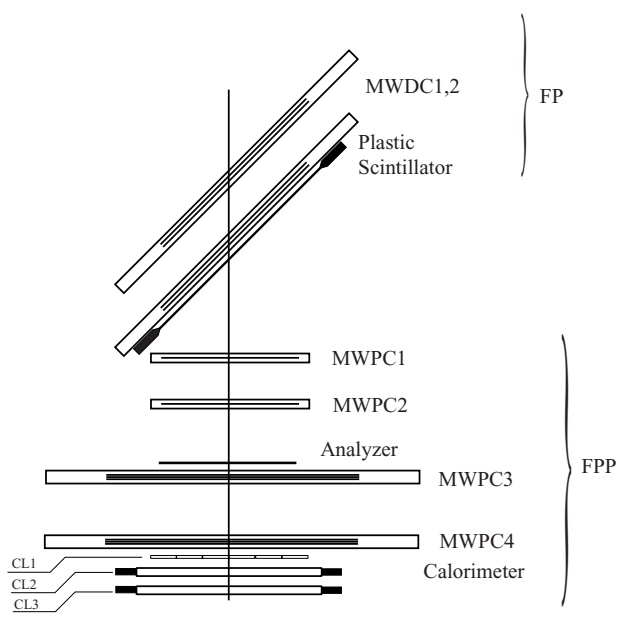

FIG. 2. Detailed configuration of the focal plane (FP) detector and the focal plane polarimeter (FPP) system.

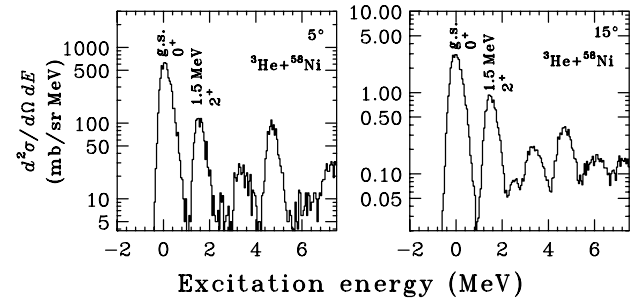

FIG. 3. Typical excitation energy spectra of ^{3}He scattering from ^{58}Ni nuclei.

order to determine the effective analyzing power of the FPP, the polarization of the ^{3}He on the analyzer target had to be determined. The absolute magnitude of the polarization was measured by the double scattering method under the time reversal invariance condition, where the polarization is equivalent to the analyzing power [42]. If the conditions of the first scattering are identical to those of the second scattering, the absolute magnitude of the polarization P_y can be obtained by measuring the left-right asymmetry in the second scattering. The absolute polarization was measured for ^{3}He+^{12}C scattering at 7° in the laboratory frame. We used a 30 mg/cm^2 thick carbon foil and a carbon sheet with a thickness of 2 mm (375 mg/cm^2) as a polarizer and an analyzer, respectively. The absolute magnitude of the polarization was determined to be

$$P_y = 0.547 \pm 0.018^{+0.019}_{-0.020}, \tag{1}$$

where the first and second uncertainties are statistical and systematic errors, respectively. The systematic uncertainties

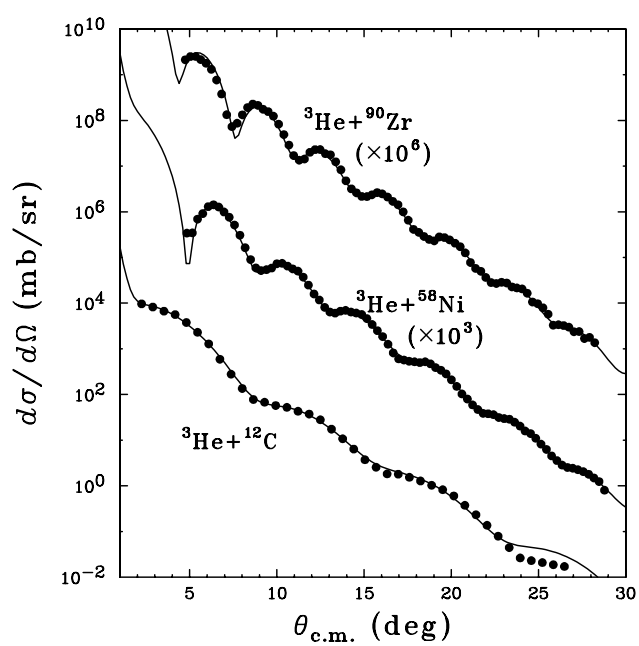

FIG. 4. Measured differential cross sections of ^{3}He elastic scattering from ^{12}C, ^{58}Ni, and ^{90}Zr at 443 MeV incident energy are represented by dots. The solid curves show the results of the optical model calculations whose parameters are given in Table II.

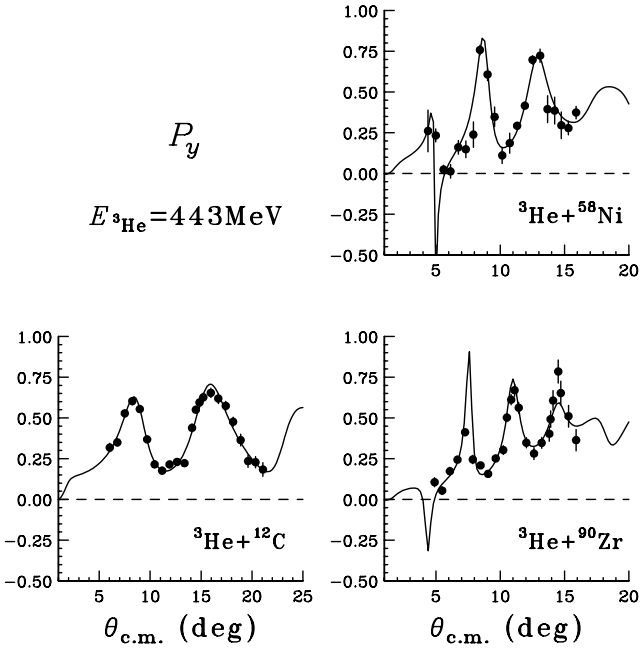

FIG. 5. The dots represent measured induced polarizations of ^{3}He elastic scattering from ^{12}C, ^{58}Ni, and ^{90}Zr at 443 MeV incident energy. The solid curves show the results of the optical model calculations whose parameters are given in Table II.

arose mainly from the uncertainty in the ^{3}He energies of the second scattering, because inelastic scattering events were not completely separated from elastic scattering events [41].

With the absolute polarization P_y known, the effective analyzing power of the FPP can be derived by

$$A_y^{eff}=\frac{1}{P_y}\varepsilon=\frac{1}{P_y}\frac{\int_L \sigma(\theta_2,\phi_2)d\Omega-\int_R \sigma(\theta_2,\phi_2)d\Omega}{\int_L \sigma(\theta_2,\phi_2)d\Omega+\int_R \sigma(\theta_2,\phi_2)d\Omega}, \tag{2}$$

where the cross section $\sigma(\theta,\phi)$ of a beam with polarization P_y is related to the cross section $\sigma_0(\theta)$ of an unpolarized beam by

$$\sigma(\theta,\phi)=\sigma_0(\theta)\{1+A_y(\theta)P_y\cos\phi\}. \tag{3}$$

The asymmetry ε was evaluated for the inclusive ^{3}He scattering from the analyzer consisting of a plastic scintillator with a thickness of 16 mm. Angular integrations in Eq. (2) were performed over $5°\leqslant\theta_2\leqslant 12°$ for the polar angle and $-60°\leqslant\phi_2\leqslant 60°$ for the azimuthal angle in the laboratory frame. The effective analyzing power was determined to be

$$A_y^{eff}=0.232\pm 0.010^{+0.017}_{-0.015}, \tag{4}$$

where the first and second uncertainties represent the statistical and systematic errors, respectively. The systematic uncertainties were estimated from those given in Eq. (1) for the absolute polarization.

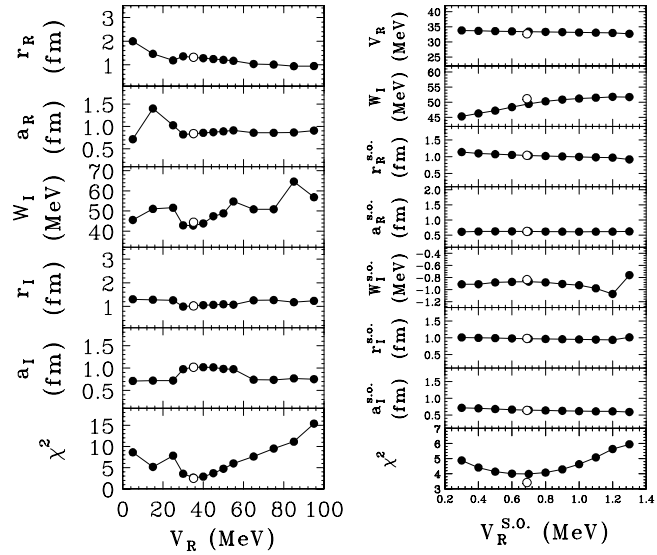

FIG. 6. Results of the systematic search to minimize χ^2 in the case of ^{3}He+^{58}Ni elastic scattering. Left panel shows the central potential parameter search for the differential cross section, while the right panel shows the spin-orbit parameter search for both the cross sections and polarizations. Open circles represent parameters for the minimum χ^2 by allowing all the parameters to be varied.

The energy dependence of the effective analyzing power was also measured by inserting an aluminum degrader downstream of the wire chamber MWDC2 in order to change the ^{3}He particles energy at the center of the analyzer [41]. The energy dependence of A_y^{eff} was taken into account in the ^{3}He elastic scattering on ^{12}C, where the A_y^{eff} varied about 6% within the measured angular range. Because the change of the A_y^{eff} was less than 1% for ^{58}Ni and ^{90}Zr nuclei, we used A_y^{eff} given by Eq. (4).

B. Cross section and induced polarization measurements

The differential cross section and the induced polarization were measured for ^{3}He+^{12}C, ^{58}Ni, and ^{90}Zr elastic scattering. Although the differential cross sections were measured previously [33], they had large statistical uncertainties at backward angles. Therefore, we measured the differential cross section again with good statistics to determine the optical potential parameters with better precision. The angular distributions of the cross section and polarization were measured from 5° to 30° and from 5° to 15° in the laboratory frame, respectively. The thicknesses of the targets were determined by weighing and were 100 mg/cm^2 for both ^{58}Ni and ^{90}Zr. We used an enriched 30-mg/cm^2-thick target ^{12}C and several natural carbon targets with thicknesses between 87 and 342 mg/cm^2. The energy straggling in the thickest target was about 700 keV. Figure 3 shows typical energy spectra of ^{3}He particles scattered from the ^{58}Ni target. In this case, the ground state was clearly separated from the first excited state.

III. EXPERIMENTAL RESULTS AND OPTICAL MODEL ANALYSIS

The measured differential cross sections $d\sigma/d\Omega$ and induced polarizations P_y in the center-of-mass system are

TABLE I. Optical potential parameters that give the minimum χ^2 in a fitting procedure of the experimental differential cross section data. The reduced χ^2 and volume integrals are also shown.

	V_R (MeV)	r_R (fm)	a_R (fm)	W_I (MeV)	r_I (fm)	a_I (fm)	χ^2	$J_{R,I}/A_PA_T$ (MeV fm^3)
^{12}C	19.73	1.592	0.705	37.76	0.989	0.868	0.35	152.2, 125.0
^{58}Ni	35.16	1.320	0.840	44.43	1.021	1.018	2.48	142.9, 109.3
^{90}Zr	31.20	1.363	0.818	42.06	1.044	1.055	5.18	129.8, 100.2

shown in Figs. 4 and 5, respectively, as closed circles together with statistical error bars. The differential cross sections for the ^{12}C target in Fig. 4 were measured previously [43]. In the present experiment, we repeated them at the same angles as the polarization measurements. Our results agreed with the previous data within statistical uncertainties.

Calculations were performed using the optical model code ECIS88/95 [44]. The optical potential was written in the Woods-Saxon form as

$$\begin{aligned} U(R) &= U_{Coul}(R) - V_R f(R;r_R,a_R) - iW_I f(R;r_I,a_I) \\ &\quad + \left(\frac{\hbar}{m_\pi c}\right)^2 \frac{1}{R}\frac{d}{dR}\{V_R^{so} f(R;r_R^{so},a_R^{so}) \\ &\quad + iW_I^{so} f(R;r_I^{so},a_I^{so})\}\boldsymbol{L}\cdot\boldsymbol{\sigma} \\ &= U_{Coul}(R) + U_R^c(R) + iU_I^c(R) + \{F_R^{so}(R) \\ &\quad + iF_I^{so}(R)\}\boldsymbol{L}\cdot\boldsymbol{\sigma}, \end{aligned} \tag{5}$$

where

$$f(R;r_i,a_i) = [1+\exp\{(R-r_iA_T^{1/3})/a_i\}]^{-1}. \tag{6}$$

The parameter A_T denotes the mass number of the target nucleus. The first term $U_{Coul}(R)$ represents the Coulomb potential between a uniformly charged sphere of radius $1.3A_T^{1/3}$ fm and a pointlike ^{3}He particle. The second and third terms represent the real and imaginary parts of the central potential, respectively. A volume type potential $-iW_If(R;r_I,a_I)$ was adopted for the imaginary central part. The fourth term includes the real and imaginary parts of the spin-orbit (SO) potential. In the present analysis, we did not include the other type of the spin-orbit force originating from the interaction between the magnetic moment of the scattered particle and the Coulomb field of the target nucleus, called the Mott-Schwinger interaction (MSI) [45] because its effects are expected to be small in our case. The MSI has been investigated for neutron scatterings from the heavy nuclei at forward angles [46,47]. The effective angular range of the MSI is inversely proportional to the particle wave number [45] and is therefore smaller than 2°, for ^{90}Zr at the present energy of 443 MeV. In the case of charged-particle elastic scattering, the polarization at forward angles is even smaller than for neutrons due to contributions from large spin-independent Coulomb scattering [48].

The potential parameters were determined by fitting the experimental data so as to minimize χ^2 divided by the number of measurements N (reduced χ-square), which is defined by

$$\chi^2 = \frac{1}{N}\sum_{i=1}^{N}\left(\frac{O_{\rm exp}(\theta_i)-O_{\rm cal}(\theta_i)}{\Delta O_{\rm exp}(\theta_i)}\right)^2, \tag{7}$$

where $O_{\rm exp}(\theta)$ denotes the experimental differential cross section or the polarization, and $O_{\rm cal}(\theta)$ the corresponding observable calculated using the optical potential given by Eq. (5). The quantity $\Delta O_{\rm exp}(\theta_i)$ is the statistical uncertainty of the experimental data. Each potential parameter was determined in the following way. At first, the central potential parameters V_R, r_R, a_R, W_I, r_I, and a_I were determined by fitting the differential cross section data. Following the procedure described in Ref. [33], minimum errors of 3% were assumed for the experimental data with statistical errors less than 3% in order to obtain an overall fit in the whole angular range. The left panel in Fig. 6 shows the results of a systematic search by minimizing the reduced χ^2 for ^{58}Ni. The real potential depth V_R was varied between 5 MeV and 95 MeV in 10-MeV steps and in fine 5-MeV steps near the minimum χ^2 value. For each real potential depth V_R, the remaining five parameters r_R, a_R, W_I, r_I, and a_I were used to minimize χ^2. The possible combinations of initial values for these five parameters were investigated by a grid search procedure in order to avoid local minima. After this systematic search, the best-fit parameters were obtained allowing all the six parameters to be varied to obtain a minimum χ^2. The open circles in the left panel of Fig. 6 show the best-fit op-

TABLE II. Optical potential parameters of the central and spin-orbit terms which give the minimum χ^2 to the experimental cross section and polarization. The reduced χ^2 for each observable and the reduced volume integrals are also shown.

	V_R (MeV)	r_R (fm)	a_R (fm)	W_I (MeV)	r_I (fm)	a_I (fm)	V_R^{so} (MeV)	r_R^{so} (fm)	a_R^{so} (fm)	W_I^{so} (MeV)	r_I^{so} (fm)	a_I^{so} (fm)	χ^2_σ	$\chi^2_{P_y}$	χ^2	J_R/A_PA_T (MeV fm^3)	J_I/A_PA_T (MeV fm^3)
^{12}C	19.14	1.600	0.702	38.06	0.999	0.869	1.10	0.945	0.790	−0.32	0.907	0.598	0.42	1.28	1.70	149.0	128.3
^{58}Ni	32.67	1.331	0.825	51.17	0.991	1.056	0.69	1.038	0.624	−0.84	0.982	0.638	1.97	1.44	3.41	134.6	121.6
^{90}Zr	29.58	1.363	0.818	47.59	1.031	1.065	0.60	1.052	0.626	−0.33	1.098	0.709	3.81	1.54	5.35	123.1	110.9

TABLE III. Best-fit spin-orbit potential parameters for $P_y+\Delta P_y^{\rm sys}$ and $P_y-\Delta P_y^{\rm sys}$.

Fitted data	$V_R^{\rm so}$ (MeV)	$r_R^{\rm so}$ (fm)	$a_R^{\rm so}$ (fm)	$W_I^{\rm so}$ (MeV)	$r_I^{\rm so}$ (fm)	$a_I^{\rm so}$ (fm)
$P_y+\Delta P_y^{\rm sys}$	0.67	1.048	0.641	−1.02	0.973	0.675
P_y-$\Delta P_y^{\rm sys}$	0.65	1.027	0.611	−0.64	1.013	0.607

tical potential parameters in this six-parameter search. Table I summarizes the parameters that gave the best fit of the differential cross section data for each target nucleus.

Subsequently, we included spin-orbit potentials to analyze both the differential cross section and the polarization data. The complex spin-orbit potentials with the full Thomas form in Eq. (5) were used. The right panel of Fig. 6 shows the results of the minimum χ^2 procedure for the complex spin-orbit potentials. A systematic search was performed by changing the real spin-orbit depth $V_R^{\rm so}$ in the 0.1-MeV step. For each $V_R^{\rm so}$ value, seven parameters V_R, W_I, $r_R^{\rm so}$, $a_R^{\rm so}$, $W_I^{\rm so}$, $r_I^{\rm so}$, and $a_I^{\rm so}$ were optimized by minimizing the χ^2 value. The central potential depths V_R and W_I in Table I, which gave the best fit to the cross section data, were used as initial values. The remaining central potential parameters r_R, a_R, r_I, and a_I were fixed to the values given in Table I. Possible combinations of spin-orbit parameters $r_R^{\rm so}$, $a_R^{\rm so}$, $W_I^{\rm so}$, $r_I^{\rm so}$, and $a_I^{\rm so}$ were investigated under the conditions that the initial values for imaginary potential parameters were the same as those of the real potential. Finally, the best-fit parameters were obtained allowing all the 12 parameters to be varied. The results are summarized in Table II. The spin-orbit potential and the central potential depths are shown as open circles in the right panel of Fig. 6. The diffuseness parameter of the spin-orbit potential was about 0.6–0.8 fm for all three nuclei at the present energy, and the anomalously small values around 0.2 fm, which was reported in studies at 33 MeV [25,49], could not describe the present data. The differential cross section and polarization calculated with the parameters in Table II are compared with experimental results in Figs. 4 and 5 showing, in general, a good agreement. We also investigated uncertainties of the spin-orbit potential parameters that could result from systematic uncertainties of the polarization $\Delta P_y^{\rm sys}$ caused by errors of A_y^{eff} in Eq. (4). The possible range of parameters was calculated assuming the largest polarization value $P_y+\Delta P_y^{\rm sys}$ and the smallest polarization $P_y-\Delta P_y^{\rm sys}$. In this procedure, the central potential parameters were fixed to the values in Table II. Table III summarizes the resulting spin-orbit parameters for the ^{3}He+^{58}Ni elastic scattering measurements. The shaded bands in Fig. 7 represent these ambiguities of the spin-orbit potentials. It is noted that the real spin-orbit potential has a smaller uncertainty than the imaginary part and is well determined by the present study.

IV. DISCUSSION

A. Volume integral of the optical potential

Figure 8 shows the incident energy dependence of the reduced volume integrals per nucleon on the optical potentials for the ^{3}He elastic scattering from ^{56}Fe and ^{58}Ni targets (left panels) and from ^{90}Zr (right panels). The upper panels show the real parts J_R/A_PA_T and the lower panels show the imaginary parts J_I/A_PA_T of the volume integrals. The horizontal axis represents the incident energies divided by the mass numbers of the projectiles. Open circles and squares in the left panels show the volume integrals for ^{58}Ni and ^{56}Fe, respectively. Open circles in the right panels show the values for ^{90}Zr. Reduced volume integrals at low energies were calculated using the shallow optical potential parameter sets. For ^{58}Ni nucleus, we refer to the results of the studies at incident energies of $E_{^3\rm He}$=37 MeV [50], 41 MeV [51], 44 MeV [52], 51 MeV [53], 83.5 MeV [54], 89 MeV, 109 MeV, and 119 MeV [32], 90 MeV [55], 217 MeV [56], 270 MeV [57], and 450 MeV [33]. The values in Ref. [52] for the ^{56}Fe nucleus at $E_{^3\rm He}$=14, 22, 34, 38, and 53 MeV were read from the figure, since numerical values were not given. For ^{90}Zr, we used the results at $E_{^3\rm He}$=109 MeV [30], 119 MeV [58], 130 MeV [59], 217 MeV [56], 270 MeV [57], and 450 MeV [33]. Open triangles show previous results obtained from the analysis of differential cross sections with the central potentials only [33]. The values corresponding to open stars in the lower panels were obtained by analyzing the present cross section data with a central potential only. The real volume integrals from the present analysis are not shown because they have nearly the same values as the following results. Closed circles show the results with the complex spin-orbit potentials given in Table II. Solid curves indicate the volume integrals of proton optical potentials that were calculated from the global parametrization for incident energies between 80 and 180 MeV [60] . Dashed curves show estimates for the proton-^{40}Ca elastic scattering from the experimental results [61]. These estimates have been introduced in previ-

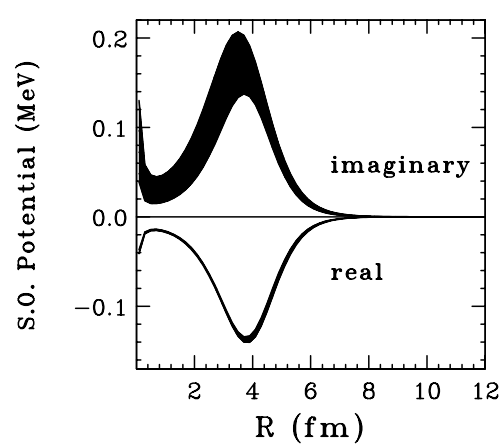

FIG. 7. The range of the spin-orbit potential due to the systematic error of P_y is shown for the ^{3}He+^{58}Ni elastic scattering.

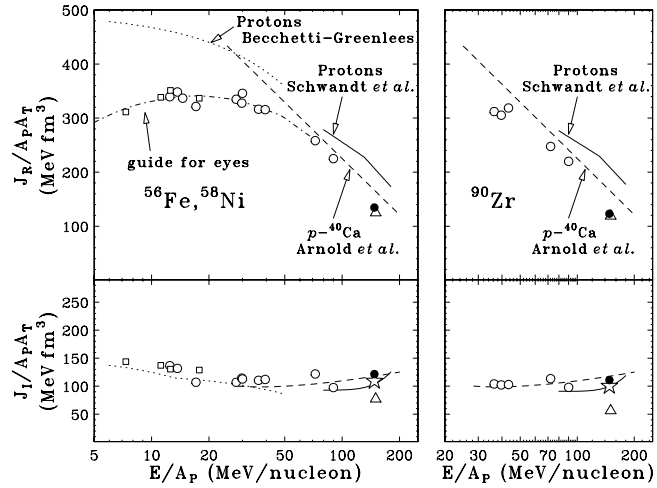

FIG. 8. The reduced volume integrals for ^{56}Fe and ^{58}Ni are shown in the panels on the left side and for ^{90}Zr on the right side as a function of the incident energy per nucleon. Open triangles represent previous results [33] obtained from the analysis of differential cross sections. The open stars in the lower panels represent J_I/A_PA_T obtained by analyzing only the cross section measured in the present experiment. The closed circles are the results of the present work obtained with the complex spin-orbit potentials. The dotted, solid, and dashed curves show the reduced volume integrals of protons. The dot-dashed curve is only meant to guide the eye.

ous works [32,33] to compare the energy dependences of $J_{R,I}/A_PA_T$ for composite particles to those for protons. Dotted curves at low energies $E_p \leqslant 50$ MeV show results for proton-nucleus scattering using the global parametrization of Becchetti and Greenlees [17]. The dot-dashed curve is meant to guide the eye.

The real volume integrals J_R/A_PA_T at 150 MeV/nucleon, which were obtained in the present work including the spin-orbit potential, are consistent with the results of a previous analysis of the differential cross section [33] with the central potentials only. On the other hand, the values of the imaginary parts J_I/A_PA_T in the previous analysis are only half of those for protons as can be seen from the open triangles in Fig. 8. The J_I/A_PA_T values from the analysis of cross sections of this work (open stars), measured up to larger scattering angles with sufficient statistics, have larger values than the previous ones and are close to those for protons.

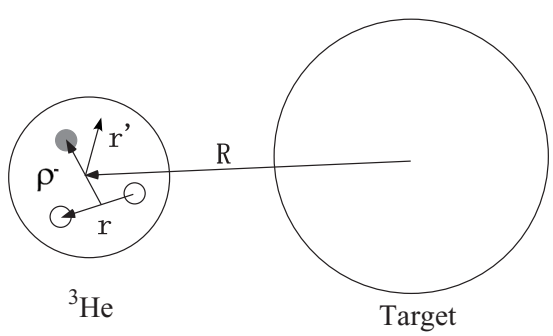

FIG. 9. Schematic representation of the Jacobi coordinates used in the SF model. The shaded circle represents an s-state neutron, while the open circles represent a pair of protons that couple to the $^1S_0$ state.

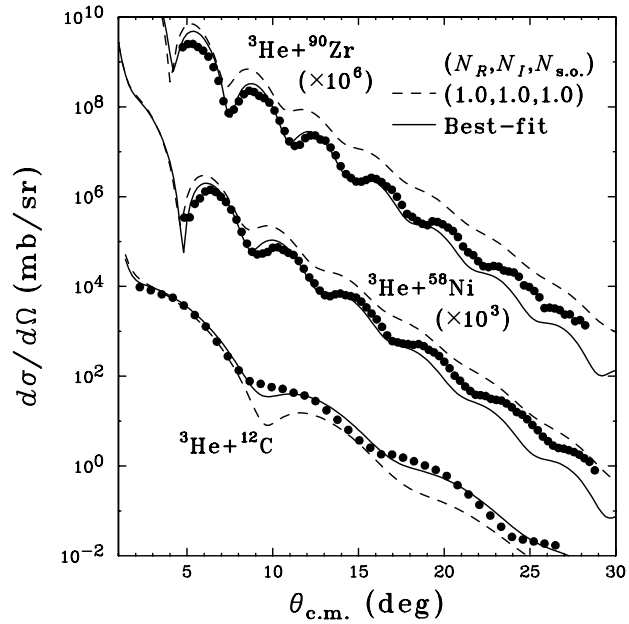

FIG. 10. Here the same data as in Fig. 4 are shown, but with the results of the SF model calculations. The dashed curves show the calculations without renormalization, while the solid curves represent the best-fit results obtained by optimizing renormalization factors.

As for the incident energy dependence of the volume integrals, the real parts J_R/A_PA_T for ^{3}He particles decrease monotonically with the incident energy above 30 MeV/nucleon. They become comparable to the values of protons at

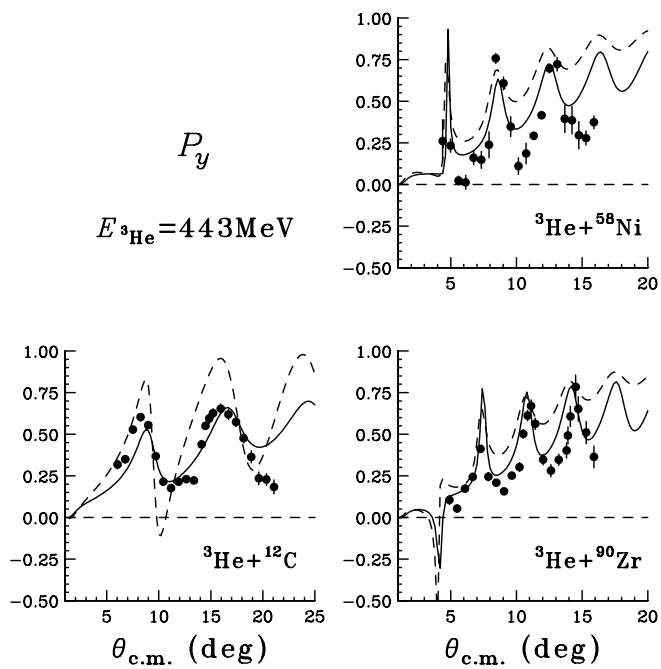

FIG. 11. The same data as in Fig. 5 are shown, but with the results of the SF model calculations. For details, see the caption of Fig. 10.

TABLE IV. The renormalization factors which give the minimum χ^2 value. The value of χ^2 and reduced volume integrals of the SF potentials after renormalization are also shown.

	N_R	N_I	N_{so}	χ^2_σ	$\chi^2_{P_y}$	χ^2	$J_{R,I}/A_PA_T$ (MeV fm^3)
^{12}C	1.59	0.80	0.58	6.39	12.69	19.08	145.5, 149.5
^{58}Ni	0.85	1.00	0.61	52.34	16.78	69.12	172.7, 105.3
^{90}Zr	0.81	1.04	0.67	83.59	9.99	93.58	166.9, 105.0

intermediate energies above 70 MeV/nucleon, where the binding energy of ^{3}He (E_B=7.72 MeV) is negligible, but they are systematically smaller than those for protons. The imaginary parts J_I/A_PA_T show the same behavior as those for protons at all energies where experimental data exist. The differences between volume integrals of the real potential of ^{3}He particles and protons could be an indication of the modification of nucleon-nucleus interactions in the ^{3}He nucleus.

B. Single folding model analysis

From above results, it is interesting to compare the experimental data with SF model calculations. In this model, the ^{3}He-nucleus interaction is obtained by folding the nucleon-nucleus interaction by the nucleon density distribution of ^{3}He [35].

The central component of the SF potential is evaluated as

$$U^{c}_{(SF)}(\boldsymbol{R}) = \int \rho_{^3\mathrm{He}}(\boldsymbol{r}')\{v^{c}(\boldsymbol{R}-\boldsymbol{r}') + iw^{c}(\boldsymbol{R}-\boldsymbol{r}')\}d\boldsymbol{r}' = U^{c}_{(SF)R}(\boldsymbol{R}) + iU^{c}_{(SF)I}(\boldsymbol{R}), \tag{8}$$

where v^c and w^c are the real and imaginary central parts of the proton-nucleus optical potential at the incident energy of $E_p = E_{^3\mathrm{He}}/3 = 150$ MeV. Proton potential parameters for ^{58}Ni and ^{90}Zr were taken from Ref. [60]. They determined parameters from a systematic analysis of data for target mass number $24 \leqslant A \leqslant 208$ at incident energies between 80 and 180 MeV. They extensively analyzed the analyzing powers, while proton optical potentials used in Ref. [35] were obtained mainly from an analysis of the differential cross sections [18]. Potential parameters for p-^{12}C at E_p=160 MeV [62] were used to calculate the folding potentials of ^{3}He-^{12}C. The function $\rho_{^3\mathrm{He}}$ in Eq. (8) represents the point nucleon density distribution of ^{3}He which is obtained by unfolding that of a proton from the charge density distribution of the ^{3}He determined by electron elastic scattering [63].

Assuming that only the s-state neutron in ^{3}He contributes to the spin-orbit SF potential, the spin-orbit component is written as

$$U^{so}_{(SF)}(\boldsymbol{R}) = \int \phi^{\dagger}_{^3\mathrm{He}}(\boldsymbol{r},\boldsymbol{\rho}) f^{so}\left(\boldsymbol{R} + \frac{2}{3}\boldsymbol{\rho}\right)\phi_{^3\mathrm{He}}(\boldsymbol{r},\boldsymbol{\rho})d\boldsymbol{r}d\boldsymbol{\rho} \times \langle \eta | \boldsymbol{l}_n \cdot \boldsymbol{\sigma}_n | \eta \rangle = \{F^{so}_{(SF)R}(\boldsymbol{R}) + iF^{so}_{(SF)I}(\boldsymbol{R})\}\boldsymbol{L}\cdot\boldsymbol{\sigma}, \tag{9}$$

where f^{so} represents the form factor of the proton $\boldsymbol{l}\cdot\boldsymbol{\sigma}$ potential at the incident energy of $E_p = E_{^3\mathrm{He}}/3$. The parameters in f^{so} were taken from the same Refs. [62,24] as those of the central potentials for each target nucleus. Since f^{so} is complex, the resulting spin-orbit component $F^{so}_{(SF)R,I}(\boldsymbol{R})$ is also complex in the SF model. The $\phi_{^3\mathrm{He}}(r,\rho)$ term represents the internal wave function of ^{3}He, while η is the product of the spin and angular parts of the wave function of the ^{3}He nucleus. We used the ^{3}He wave function in a Gaussian form [64]. The vectors $\boldsymbol{r}$ and $\boldsymbol{\rho}$ are the relative coordinates between two protons and between the neutron and the center of mass of the two protons in ^{3}He, respectively. The schematic representation of the Jacobi coordinates is shown in Fig. 9. The orbital angular momentum and the Pauli spin operator of the neutron in ^{3}He are denoted by $\boldsymbol{l}_n$ and $\boldsymbol{\sigma}_n$, respectively, while the corresponding operators in the ^{3}He-target system are represented by $\boldsymbol{L}$ and $\boldsymbol{\sigma}$.

The total SF potential reads

$$U_{(SF)}(R) = U_{Coul}(R) + N_R U^{c}_{(SF)R}(R) + iN_I U^{c}_{(SF)I}(R) + N_{so}\{F^{so}_{(SF)R}(R) + iF^{so}_{(SF)I}(R)\}\boldsymbol{L}\cdot\boldsymbol{\sigma}, \tag{10}$$

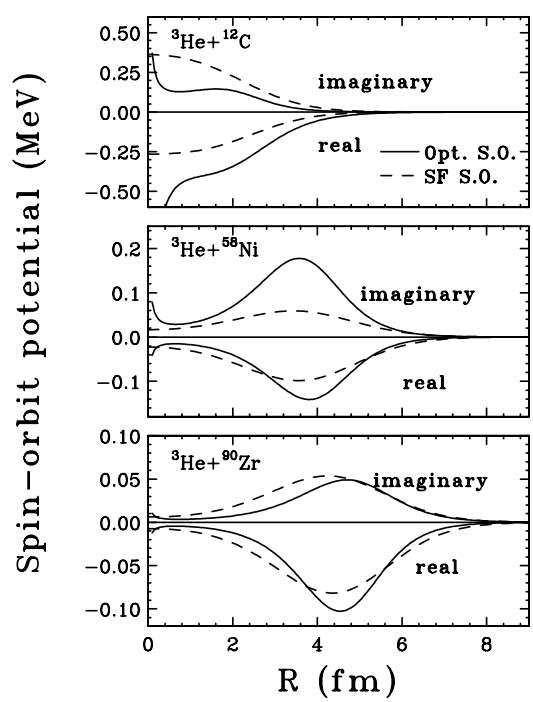

FIG. 12. Comparison of the spin-orbit potentials of optical model with those of SF model. Solid and dashed curves are the results of the optical model and SF model, respectively.

where the renormalization factors (N_R, N_I, N_{so}) are introduced to modify the strength of the corresponding term.

In Figs. 10 and 11, calculated differential cross sections and induced polarizations with the SF potentials are compared with the experimental data, respectively. The dashed curves are predictions without renormalization, i.e., $N_R = N_I = N_{so} = 1$. The solid curves are the best-fit results allowing the renormalization factors to be varied in order to minimize the χ^2 value. Resulting renormalization factors are summarized in Table IV together with reduced volume integrals.

The SF model calculations without renormalization overestimated the experimental cross sections for ^{58}Ni and ^{90}Zr. Thus, the real central terms had to be modified by 15–20 % to obtain best-fits, while the imaginary central potentials did not need to be modified. The volume integrals of the real SF potential for ^{58}Ni and ^{90}Zr were $J_R/A_P A_T = 203$ and 206, respectively, without renormalization. These values were renormalized to 173 and 167, respectively. The differences of $J_R/A_P A_T$ from protons described in Sec. IV A were partly compensated by renormalization. For ^{12}C, the optimum renormalization factors were very different from the other, heavier nuclei. The real potential was strengthened by 60% and the imaginary potential was reduced by 20%. This might result from the fact that the p-^{12}C optical potential is usually not well described by the global parametrization. The SF spin-orbit potentials were reduced by 30–40 % to give best fits for all nuclei. The spin-orbit optical potentials are shown in Fig. 12 and are compared with the SF potentials. It can be seen that the optical potentials do not have sharp peaks at the surface, unlike at low energies [26], but they have broad shapes similar to the SF potentials. By introducing the renormalization factors the experimental data were generally well reproduced, except for the cross section at backward angles for ^{58}Ni and ^{90}Zr, where the calculations underestimated the data. Such a discrepancy was also reported in a previous analysis [35]. The necessity of renormalization may be attributed to the fact that the SF potential does not include any density dependence of the nucleon-nucleus interaction in the ^{3}He nucleus. A DF model with density dependent effective interactions was recently applied to ^{3}He elastic scattering [35,65]. The resulting renormalization factors were close to unity when the density dependence of the effective *NN* interactions was properly taken into account. The above discussion of the SF model is consistent with the conclusions of the DF model.

V. SUMMARY AND CONCLUSION

The angular distributions of differential cross sections and induced polarizations for ^{3}He elastic scattering from ^{12}C, ^{58}Ni, and ^{90}Zr targets were measured at an incident energy of $E_{^3\mathrm{He}} = 443$ MeV. Cross sections were measured at laboratory angles $5° < \theta_{\mathrm{lab}} < 30°$ and polarization parameters at $5° < \theta_{\mathrm{lab}} < 15°$. The polarization was measured using the focal plane polarimeter system of the Grand Raiden spectrometer that was calibrated for ^{3}He at the present energy.

The optical potential parameters including the spin-orbit term were determined by a systematic analysis. Resulting optical model calculations described well both the experimental cross sections and polarizations. The diffuseness parameter of the spin-orbit potential was about 0.6–0.8 fm, which was similar to the values for protons in contrast to the much smaller values reported at lower energies. Volume integrals of the central potentials showed a similar energy dependence compared to protons above 70 MeV/nucleon, although the real terms were smaller than those for protons. The SF model predictions were compared with the experimental data. The SF potentials had to be renormalized in order to reproduce the experimental data well. It may be necessary to take into account the density dependence of the nucleon-nucleus interaction in the ^{3}He nucleus. It is interesting to compare the present data to theoretical predictions of the double folding model employing density dependent effective interactions.

This is the first measurement of polarization observables of ^{3}He-nucleus scattering at intermediate energies. In order to investigate spin-dependent nucleus-nucleus interaction, it is important to make systematic studies in a wider energy region. However, it is difficult to design an efficient ^{3}He polarimeter system for a wide range of energies. The development of a polarized ^{3}He ion source would provide good opportunities to extend the present study as well as to make an absolute calibration of the polarimeter system.

ACKNOWLEDGMENTS

We gratefully acknowledge the support of all RCNP staff members during the experiment. We thank Professor Y. Sakuragi and Dr. M. Katsuma for helpful discussions and many important comments. We also thank Professor H. Toki for his encouragement throughout this work. We are grateful to Dr. G. P. A. Berg for his critical reading of the manuscript. This experiment was performed under Programs Nos. E157, E182, and R38 at the RCNP and supported in part by the Grant-in-Aid for Scientific Research, Grant No. 14340074, of the Ministry of Education, Culture, Sports, Science and Technology of Japan.

[1] V.G.J. Stoks, R.A.M. Klomp, C.P.F. Terheggen, and J.J. de Swart, Phys. Rev. C **49**, 2950 (1994).

[2] R.B. Wiringa, V.G.J. Stoks, and R. Schiavilla, Phys. Rev. C **51**, 38 (1995).

[3] R. Machleidt, F. Sammarruca, and Y. Song, Phys. Rev. C **53**, R1483 (1996).

[4] K. Sekiguchi, H. Sakai, H. Witała, W. Glöckle, J. Golak, M. Hatano, H. Kamada, H. Kato, Y. Maeda, J. Nishikawa, A. Nogga, T. Ohnishi, H. Okamura, N. Sakamoto, S. Sakoda, Y. Satou, K. Suda, A. Tamii, T. Uesaka, T. Wakasa, and K. Yako,

Phys. Rev. C **65**, 034003 (2002).
[5] K. Hatanaka, Y. Shimizu, D. Hirooka, J. Kamiya, Y. Kitamura, Y. Maeda, T. Noro, E. Obayashi, K. Sagara, T. Saito, H. Sakai, Y. Sakemi, K. Sekiguchi, A. Tamii, T. Wakasa, Y. Yagita, K. Yako, H.P. Yoshida, V.P. Ladygin, H. Kamada, W. Glöckle, J. Golak, A. Nogga, and H. Witała, Phys. Rev. C **66**, 044002 (2002).
[6] G. Bertsch, J. Borysowicz, H. McManus, and W.G. Love, Nucl. Phys. **A284**, 399 (1977).
[7] D.W.L. Sprung and P.K. Banerjee, Nucl. Phys. **A168**, 273 (1971).
[8] N. Anantaraman, H. Toki, and G.F. Bertsch, Nucl. Phys. **A398**, 269 (1983).
[9] F. Petrovich, D. Stanley, and J.J. Bevelacqua, Phys. Lett. **71B**, 259 (1977).
[10] B. Sinha, F. Duggan, and R.J. Griffiths, Nucl. Phys. **A241**, 229 (1975).
[11] A.M. Kobos, B.A. Brown, P.E. Hodgson, G.R. Satchler, and A. Budzanowski, Nucl. Phys. **A384**, 65 (1982).
[12] A.M. Kobos, B.A. Brown, R. Lindsay, and G.R. Satchler, Nucl. Phys. **A425**, 205 (1984).
[13] L.D. Rickertsen and G.R. Satchler, Phys. Lett. **66B**, 9 (1977).
[14] W.G. Love, Phys. Lett. **72B**, 4 (1977).
[15] D.T. Khoa and W. von Oertzen, Phys. Lett. B **342**, 6 (1995).
[16] D.T. Khoa, G.R. Satchler, and W. von Oertzen, Phys. Rev. C **56**, 954 (1997).
[17] F.D. Becchetti, Jr. and G.W. Greenlees, Phys. Rev. **182**, 1190 (1969).
[18] A. Nadasen, P. Schwandt, P.P. Singh, W.W. Jacobs, A.D. Bacher, P.T. Debevec, M.D. Kaitchuck, and J.T. Meek, Phys. Rev. C **23**, 1023 (1981).
[19] S. Hama, B.C. Clark, E.D. Cooper, H.S. Sherif, and R.L. Mercer, Phys. Rev. C **41**, 2737 (1990).
[20] H. Sakaguchi, H. Takeda, S. Toyama, M. Itoh, A. Yamagoshi, A. Tamii, M. Yosoi, H. Akimune, I. Daito, T. Inomata, T. Noro, and Y. Hosono, Phys. Rev. C **57**, 1749 (1998).
[21] K. Hatanaka, K. Imai, S. Kobayashi, T. Matsusue, M. Nakamura, K. Nisimura, T. Noro, H. Sakamoto, H. Shimizu, and J. Shirai, Nucl. Phys. **A340**, 93 (1980).
[22] M. Yahiro, Y. Iseri, H. Kameyama, M. Kamimura, and M. Kawai, Prog. Theor. Phys. Suppl. **89**, 32 (1986).
[23] D. Fick, R.E. Brown, W. Grüebler, R.A. Hardekopf, and J.S. Hanspal, Phys. Rev. C **29**, 324 (1984).
[24] P. Schwandt, R.E. Brown, F.D. Correll, R.A. Hardekopf, and G.G. Ohlsen, Phys. Rev. C **26**, 369 (1982).
[25] S. Roman, A.K. Basak, J.B.A. England, O. Karban, G.C. Morrison, and J.M. Nelson, Nucl. Phys. **A284**, 365 (1977).
[26] J.S. Hanspal, R.J. Griffiths, N.M. Clarke, J.M. Barnwell, O. Karban, and S. Roman, Nucl. Phys. **A427**, 297 (1984).
[27] S.P.V. Verst, D.P. Sanderson, D.E. Trcka, K.W. Kemper, V. Hnizdo, B.G. Schmidt, and K.R. Chapman, Phys. Rev. C **39**, 853 (1989).
[28] G. Tungate, D. Krämer, R. Butsch, O. Karban, K.H. Möbius, W. Ott, P. Paul, A. Weller, E. Steffens, K. Becker, K. Blatt, D. Fick, B. Heck, H. Jänsch, H. Leucker, K. Rusek, I.M. Turkiewicz, and Z. Moroz, J. Phys. G **12**, 1001 (1986).
[29] J.S. Hanspal, K.I. Pearce, N.M. Clarke, R.J. Griffiths, R.E. Brown, R.A. Hardekopf, and W. Grüebler, Nucl. Phys. **A455**, 494 (1986).
[30] M. Hyakutake, M. Matoba, I. Kumabe, M. Fukada, T. Komatuzaki, T. Yamagata, M. Tanaka, M. Inoue, I. Miura, and H. Ogata, Nucl. Phys. **A311**, 161 (1978).
[31] G.R. Satchler, *Direct Nuclear Reactions* (Clarendon Press, Oxford/Oxford University Press, New York, 1983), p. 500.
[32] M. Matoba, M. Hyakutake, and I. Kumabe, Phys. Rev. C **32**, 1773 (1985).
[33] T. Yamagata, H. Utsunomiya, M. Tanaka, S. Nakayama, N. Koori, A. Tamii, Y. Fujita, K. Katori, M. Inoue, M. Fujiwara, and H. Ogata, Nucl. Phys. **A589**, 425 (1995).
[34] G.R. Satchler and W.G. Love, Phys. Rep. **55**, 183 (1979).
[35] Y. Sakuragi and M. Katsuma, Nucl. Instrum. Methods Phys. Res. A **402**, 347 (1998).
[36] M. Fujiwara, H. Akimune, I. Daito, H. Fujimura, Y. Fujita, K. Hatanaka, H. Ikegami, I. Katayama, K. Nagayama, N. Matsuoka, S. Morinobu, T. Noro, M. Yoshimura, H. Sakaguchi, Y. Sakemi, A. Tamii, and M. Yosoi, Nucl. Instrum. Methods Phys. Res. A **422**, 484 (1999).
[37] T. Wakasa, K. Hatanaka, Y. Fujita, G.P.A. Berg, H. Fujimura, H. Fujita, M. Itoh, J. Kamiya, T. Kawabata, K. Nagayama, T. Noro, H. Sakaguchi, Y. Shimbara, H. Takeda, K. Tamura, H. Ueno, M. Uchida, M. Uraki, and M. Yosoi, Nucl. Instrum. Methods Phys. Res. A **482**, 79 (2002).
[38] H. Fujita, Y. Fujita, G.P.A. Berg, A.D. Bacher, C.C. Foster, K. Hara, K. Hatanaka, T. Kawabata, T. Noro, H. Sakaguchi, Y. Shimbara, T. Shinada, E.J. Stephenson, H. Ueno, and M. Yosoi, Nucl. Instrum. Methods Phys. Res. A **484**, 17 (2002).
[39] M. Yosoi, H. Akimune, I. Daito, M. Fujiwara, S. Hirata, T. Inomata, O. Kamigaito, M. Kawabata, T. Noro, Y. Sakemi, T. Takahashi, A. Tamii, S. Toyama, A. Yamagoshi, M. Yoshimura, and H. Sakaguchi, in *High Energy Spin Physics*, edited by K. J. Heller and S. L. Smith, AIP Conf. Proc. No. 343 (AIP, Woodbury, NY, 1995), p. 157.
[40] T. Noro, M. Fujiwara, O. Kamigaito, S. Hirata, Y. Fujita, A. Yamagoshi, T. Takahashi, H. Akimune, Y. Sakemi, M. Yosoi, H. Sakaguchi, and J. Tanaka, RCNP Annual report, 1991, p. 177.
[41] J. Kamiya *et al.*, Nucl. Instrum. Methods Phys. Res. A (to be published).
[42] G.G. Ohlsen, Rep. Prog. Phys. **35**, 717 (1972).
[43] H. Fujimura, Ph.D. thesis, Osaka University, 2002.
[44] J. Raynal, computer code ECIS-88 NEA-0850/08; computer code ECIS-88 NEA-0850/14.
[45] J. Schwinger, Phys. Rev. **73**, 407 (1948).
[46] R.B. Galoway and R.M.A. Maayouf, Nucl. Instrum. Methods **105**, 561 (1972).
[47] R.M.A. Maayouf and R.B. Galoway, Phys. Rev. **118**, 343 (1974).
[48] W. Heckrotte, Phys. Rev. **101**, 1406 (1956).
[49] W.E. Burcham, J.B.A. England, R.G. Harris, O. Karban, and S. Roman, Nucl. Phys. **A246**, 269 (1975).
[50] P.P. Urone, L.W. Put, B.W. Ridley, and G.D. Jones, Nucl. Phys. **A167**, 383 (1971).
[51] H.-J. Trost, A. Schwarz, U. Feindt, F.H. Heimlich, S. Heinzel, J. Hintze, F. Körber, R. Lekebusch, P. Lezoch, G. Möck, W. Paul, E. Roick, M. Wolff, J. Worzeck, and U. Strohbusch, Nucl. Phys. **A337**, 377 (1980).
[52] C.J. Marchese, N.M. Clarke, and R.J. Griffiths, Phys. Rev. Lett. **29**, 660 (1972).

[53] C.R. Bingham and M.L. Halbert, Phys. Rev. **169**, 933 (1968).
[54] H.H. Chang, B.W. Ridley, T.H. Braid, T.W. Conlon, E.F. Gibson, and N.S.P. King, Nucl. Phys. **A297**, 105 (1978).
[55] N. Matsuoka, K. Hatanaka, M. Fujiwara, Y. Fujita, T. Saito, K. Hosono, A. Shimizu, M. Kondo, F. Ohtani, H. Sakaguchi, A. Goto, N. Nakanishi, and Y. Toba, Nucl. Phys. **A373**, 377 (1982).
[56] N. Willis, I. Brissaud, Y. Le Bornec, B. Tatischeff, and G. Duhamel, Nucl. Phys. **A204**, 454 (1973).
[57] P.P. Singh, Q. Li, P. Schwandt, W.W. Jacobs, M. Saber, E.J. Stephenson, A. Saxena, and S. Kailas, Pramana **27**, 747 (1986).
[58] M. Hyakutake, I. Kumabe, M. Fukada, T. Komatuzaki, T. Yamagata, M. Inoue, and H. Ogata, Nucl. Phys. **A333**, 1 (1980).
[59] A. Djaloeis, J.-P. Didelez, A. Galonsky, and W. Oelert, Nucl. Phys. **A306**, 221 (1978).
[60] P. Schwandt, H.O. Meyer, W.W. Jacobs, A.D. Bacher, S.E. Vigdor, M.D. Kaitchuck, and T.R. Donoghue, Phys. Rev. C **26**, 55 (1982).
[61] L.G. Arnold, B.C. Clark, E.D. Cooper, H.S. Sherif, D.A. Hutcheon, P. Kitching, J.M. Cameron, R.P. Liljestrand, R.N. MacDonald, W.J. McDonald, C.A. Miller, G.C. Neilson, W.C. Olsen, D.M. Sheppard, G.M. Stinson, D.K. McDaniels, J.R. Tinsley, R.L. Mercer, L.W. Swensen, P. Schwandt, and C.E. Stronach, Phys. Rev. C **25**, 936 (1982).
[62] H.O. Meyer, P. Schwandt, W.W. Jacobs, and J.R. Hall, Phys. Rev. C **27**, 459 (1983).
[63] H. D Vries, C.W. D Jager, and C. D Vries, At. Data Nucl. Data Tables **36**, 495 (1987).
[64] S.K. Samaddar, R.K. Satpathy, and S. Mukherjee, Nucl. Phys. **A150**, 655 (1970).
[65] M. Katsuma *et al.* (unpublished).